Nanoscale

Accepted Manuscript

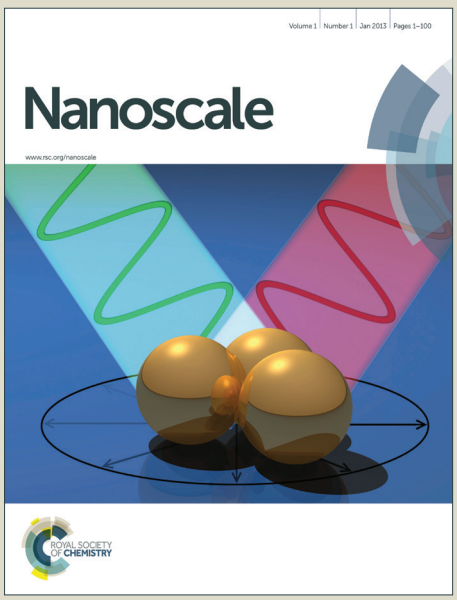

ROYAL SOCIETY OF CHEMISTRY

www.rsc.org/nanoscale

Cite this: DOI: 10.1039/c0xx00000x

www.rsc.org/xxxxxx

ARTICLE TYPE

Surface-Enhanced Spectroscopy on Plasmonic Oligomers Assembled by AFM Nanoxerography

Pierre Moutet[a], Neralagatta M. Sangeetha[a], Laurence Ressier[a], Noélia Vilar-Vidal[b], Miguel Comesaña[b], Serge Ravaine[b], Renaud A. L. Vallée[b],Ana Maria Gabudean[c], Simion Astilean[c], Cosmin Farcau[c]*

Received (in XXX, XXX) XthXXXXXXXXX 20XX, Accepted Xth XXXXXXXXX 20XX
DOI: 10.1039/b000000x

Surface enhanced Raman scattering (SERS) and surface enhanced fluorescence (SEF) from individual plasmonic oligomers are investigated by confocal Raman micro-spectroscopy and time-resolved fluorescence microscopy coupled to steady state micro-spectroscopy. The nanoparticle (NP) oligomers are made of either ligand protected Au or Au@SiO_2 core-shell colloidal NPs, which were assembled into ordered arrays by atomic force microscopy (AFM) nanoxerography. A strong dependence of the SERS emission on the polarization of incident light relative to the specific geometry of the plasmonic oligomer was observed. The SEF studies, performed on a large collection of NP oligomers of various known configurations, showed interesting fluorophore decay rate modification and red-shift of the emission spectra. Experimental results are analyzed theoretically, by employing finite-difference time-domain (FDTD) simulations on equivalent realistic structures, within the Local Density of Optical States (LDOS) framework. The presented results, together with the proven potential of the LDOS approach as a useful common tool for analyzing both SERS and SEF effects, furthers the general understanding of plasmon-related phenomena in nanoparticle oligomers.

Introduction

The possibility to confine and manipulate light at the nanoscale by means of surface plasmons allows the observation of interesting phenomena such as Fano resonances,[1] enhanced optical transmission,[2] plasmon-induced transparency,[3] unidirectional fluorescence emission,[4] or surface plasmon lasing,[5] to name a few. Such observations are bringing about rapid advancements in the field of plasmonics, both at the fundamental and application level.

On the one hand, many applications based on the unique properties of surface plasmons have been proposed in areas ranging from optical spectroscopy,[6–9] energy[10] and materials processing,[11] to communications.[12] A major class of plasmonics applications that has shown potential to reach maturity is constituted by plasmon-enhanced optical spectroscopy techniques: Raman scattering, benefiting from plasmons through Surface Enhanced Raman Scattering (SERS), fluorescence and infrared absorption with their plasmon-enhanced correspondents, Surface Enhanced Fluorescence (SEF) and Surface Enhanced IR Absorption (SEIRA). SERS is a particularly attractive tool as it enables ultrasensitive detection of analytes, down to the single molecule, and provides structural characteristics of the molecular system under study (i.e., the vibrational spectra as a fingerprint).[13,14] This makes SERS a very a promising tool to develop optical sensors for detecting and analyzing bio-chemical species (medical specimen, pollutants, etc.).[15] SEF not only has similar sensing application potential,[9,16,17] but is also useful to improve the performance of optoelectronic devices, as the surface plasmon enhancement can lower the threshold in lasing,[18] or improve the efficiency of light-emitting diodes.[19,20] On the other hand, it can be argued that both SERS and SEF have also contributed to the recent understanding of the plasmonic properties of nanostructures and their interactions with optical molecular probes. Recent results have indicated that plasmon resonances have a strong effect on the SERS scattered photons, i.e. plasmons can control the polarization of the SERS emission, independently of the polarization of the excitation field.[19,20] Similarly, surface plasmons have been demonstrated to modulate both the intensity and shape of the emission spectrum.[23,24] Indeed, these secondary radiation processes (SERS and SEF) fundamentally share the same enhancement mechanisms in the weak light-matter coupling regime.[25,26] While it is usual to consider the photon local density of states (LDOS) effect pioneered by Purcell[27] to describe the spontaneous emission processes, the effects of the LDOS on Raman scattering is ignored by many authors.[28]

Building nanoparticle (NP) oligomers (i. e. clusters made of a small number of particles) provides a great means for achieving control over surface plasmon resonances,[29] which is important for controlling SERS and SEF. Modification of the plasmon resonance of individual NPs by near-field coupling is a well-known phenomenon.[30] This coupling also leads to the generation of enhanced electromagnetic fields at the interparticle gaps, which play a major role in enhancing light-molecule interactions,

such as Raman scattering or fluorescence emission for example. The study of plasmon-enhanced SERS/SEF effects from individual NP oligomers of known geometry and composition therefore becomes crucial for understanding the underlying physico-chemical phenomena. Colloidal NPs are very appealing building blocks for constructing NP oligomers, since chemical synthesis offers versatile routes to produce both silver and gold NPs of different sizes, shapes (spheres, rods, cubes, pyramids, prisms), chemical composition (alloy or core-shell) with variable surface functionalities.[31] Another advantage of chemically synthesized NPs is their surface quality. These are typically smooth, can be monocrystalline and possess less defects compared to the nano-objects fabricated by top-down techniques. But, chemically synthesized NPs need to be assembled on solid substrates, in order to evaluate their individual or oligomer collective plasmonic properties. Achieving this in a controlled manner is highly challenging. For this, we have used here nanoxerography by atomic force microscopy (AFM), which has recently emerged as a versatile method for colloid assembly, directly from their liquid phase onto solid substrates at predefined positions.[32–40] This technique is a nanoscale adaptation of the industrial printing process of xerography. It uses the strong electric fields generated by charge patterns written on electret thin films by AFM, to trap any charged and/or polarisable colloidal NPs on solid templates via electrostatic interactions.

In this article, we present arrays of few-nanoparticle clusters (oligomers) fabricated by AFM nanoxerography and investigate selected individual oligomers of different sizes and configurations, by confocal Raman micro-spectroscopy and time-resolved confocal fluorescence microscopy. The NP oligomer arrays were constructed from organic ligand protected gold nanoparticles (Au@TDSP) and Au@SiO_2@dye core-shell nanoparticles (Au@SiO_2@Rhodamine B), specifically designed for SERS and SEF studies, respectively. Finite-Difference Time-Domain simulations have been performed on realistic structures mimicking the configurations of the actual oligomers observed by AFM. Finally, the simulation results are correlated to the experimental ones and analyzed within the LDOS framework.

Materials and Methods

Materials

Tris(2,4-dimethyl-5-sulfonatophenyl)phosphine (TDSP), tetraethoxysilane (TEOS), gold chloride trihydrate ($HAuCl_4 \cdot 3H_2O$), trisodium citrate dihydrate, Rhodamine B-isothiocyanate, aminopropyltriethoxysilane (APTES), and O-[2-(3-mercaptopropionylamino)ethyl] -O′-methylpolyethylene glycol (mPEG-SH) were purchased from Sigma-Aldrich. Absolute ethanol was obtained from VWR and ammonia (30 %) from Carlo-Erba. Cresyl Violet was purchased from Merck. All materials were used as received without further purification. MiliQ water was used in all of the preparations.

Chemical synthesis of Au@TDSP nanoparticles

(i) Synthesis of Au NPs. 100 nm spherical Au NPs were synthesized by a seeded growth method adapted from a published procedure,[39] and consists of three steps. In the first step, 15 ± 1 nm citrate stabilized Au NPs were synthesized by the Turkevich-Frens method. Detailed procedure for this synthesis is described elsewhere[42]. In the second step, 33 ± 3 nm Au NPs were grown using 15 ± 1 nm citrate Au NPs as seeds, as follows: 3 ml of as-prepared 15 nm citrate Au NP suspension was diluted to 20 mL with water and 10 mL of $HAuCl_4$ solution (0.04 mg/mL) and 10 mL of a reducing solution containing sodium citrate (0.05 mg/mL) and ascorbic acid (0.025 mg/mL) were added dropwise and simultaneously, under vigorous stirring over a period of 15-20 min. Immediately after the completion of addition, the reaction mixture was boiled for about 30 min. The resulting red-coloured suspension was then cooled to room temperature and stored as such. In the final step, 2 mL of the as-prepared 33 ± 3nm Au NP suspension was diluted to 5 mL with water. Immediately after this, the afore mentioned growth procedure was repeated, using the same quantities of reagents. The resulting mixture was then refluxed for 20 min to obtain a brownish red suspension.

(ii) Functionalization of Au NPs with TDSP. These Au NPs, used for SERS, were then coated with a molecular monolayer, to ensure constant and small (1-2 nm) gaps within the oligomers. For this, the particles were subjected to ligand exchange by treating the suspension with 4 mg of TDSP and refluxing the resulting mixture overnight. The TDSP protected Au NPs were then concentrated by centrifugation (3000 rpm, 10 min) and incubated again with TDSP (2–3 mg) for 2–3 h at room temperature, to ensure complete exchange of the surface ligands. Subsequently, the suspensions were diluted 10 times with de-ionized water and recentrifuged to remove excess ligand. The Au NPs sediment as a brown-red concentrate which was subsequently redispersed with deionized water to a final concentration of 3-4 mL and stored as such.

Zeta potential measurements showed that these Au@TDSP nanoparticles carried a net negative charge. Transmission electron microscopy (TEM) analysis gave a mean particle size of 102 ± 7 nm. Characterizations of the colloidal suspensions (TEM images, size histograms and optical extinction spectra) are provided in the Electronic Supplementary Information (ESI) (Figure SI-1).

Chemical synthesis of Au@SiO_2@Rhodamine B nanoparticles

(i) Synthesis of Au@SiO_2 core-shell NPs. Spherical Au NPs of 50 nm diameter were first synthesized using the standard sodium citrate reduction method.[43] Then, 2 mL of a freshly prepared aqueous solution of mPEG-SH (36.5 µM) was added dropwise to 40 mL of as-prepared AuNPs under vigorous magnetic stirring and the mixture reacted for 30 min, ensuring the replacement of the citrate molecules adsorbed onto the gold surface by mPEG-SH. Subsequently, the suspension was centrifuged at 5000 rpm for 20 min (twice) in order to eliminate the excess of mPEG-SH and the precipitate obtained was redispersed in 2 mL of EtOH. Silica (SiO_2) coating was performed following a previously reported method.[44] The concentrations of Au/TEOS/NH_3/H_2O were: 0.5 mM/0.8 mM/0.2 M/10.55 M. Au@mPEG-SHNPs were added into 13.9 mL of EtOH, followed by the addition 3.8 mL of H_2O, 253 µL of aq. NH_3 (30 %) and 101 µL of a TEOS solution in EtOH (0.16 µM). The reaction mixture was stirred for 14 h, and the resulting Au@SiO_2 core-shell NPs were purified by centrifugation at 4500 rpm for 30 min (twice) and redispersed in 5 mL of EtOH.

(ii) Functionalization of Au@SiO_2 core-shell NPs with Rhodamine B. First, Rhodamine B-isothiocyanate was

functionalized with APTES to endow the fluorophore with a silane coupling group that ensures a strong covalent bond with the $Au@SiO_2$NPs.[45,46] This functionalization was carried out as follows: 100 mg of Rhodamine B-isothiocyanate was added to 100 mL of EtOH under N_2 atmosphere, together with 44 µL of APTES. The mixture was stirred for 24 h. Then, the suspension was concentrated on a rotary evaporator, obtaining a suspension with a final concentration of 1.5 g/L which was stored in a refrigerator, under N_2. Subsequently, 5 mL of the previously synthesized $Au@SiO_2$ NPs were added to 130 mL of EtOH, followed by 220 µL of Rhodamine B-APTES complex and 8 mL of aq. NH_3 (30 %), in this order. This mixture was stirred for 1h at room temperature and another hour at 80°C. Finally, the suspension was concentrated (evaporating ca. 50 % of the original volume) and then centrifuged (5000 rpm/15 min, twice). The final precipitate was redispersed in 5 mL of EtOH.

Zeta potential measurements showed that these $Au@SiO_2$@Rhodamine B nanoparticles carried a net positive charge. The $Au@SiO_2$ NPs have an Au core of about 50±5 nm, and a silica shell about 20±2 nm thick which plays the role of preventing well-known fluorescence quenching issues. Rhodamine B molecules are grafted on the outer surface. Further characterizations of the colloidal NP suspensions (transmission electron microscopy images, size histograms, and optical extinction spectra) are provided in the ESI (Figure SI-2).

AFM nanoxerography

Figure 1 presents the two-step protocol of AFM nanoxerography used in this work. In the first step, charge dots were written onto a 100 nm thick polymethylmethacrylate (PMMA) spin-coated on 10^{16} cm^{-3} p-doped silicon substrate, by applying voltage pulses to a highly n-doped silicon AFM tip, using an external generator. The z-feedback was adjusted to control the tip-sample distance during charge writing. The pulse length and frequency were chosen at 1 ms and 50 Hz, respectively, while the time on each charge dot was fixed at 180 ms. These specific writing conditions are reliable and reproducible, causing no tip and/or sample damage at the high voltages used, as demonstrated previously.[37] After AFM charge writing, the surface potential of the charge dots was systematically measured by the electrical derived mode of amplitude modulation Kelvin Force Microscopy (KFM). For generating oligomers of negatively charged Au@TDSP NPs, positive charge dots were written to trap these particles through Coulomb forces. Likewise, negative charge dots were used for creating oligomers of positively charged $Au@SiO_2$@Rhodamine B NPs. In the second step, a 30 µL droplet of the desired colloidal suspension was incubated on the electrostatically patterned substrate for 30 s. In case of Au@TDSP NPs dispersed in water, the substrates were subsequently immersed in absolute ethanol for 30 s and rinsed with pure water, following a two-step protocol previously developed by our group, for aqueous colloidal suspensions.[38] For $Au@SiO_2$@Rhodamine NPs dispersed in EtOH, the incubation of the colloidal suspension was simply followed by rinsing in absolute ethanol. In all cases, the samples were finally dried under nitrogen flow to remove any traces of solvent. This second step lead to the selective electrostatic trapping of the charged colloidal NPs on the charge dots, generating arrays of oligomers. The number and configuration of the nanoparticle arrangement within these oligomers were determined by AFM imaging in tapping mode.

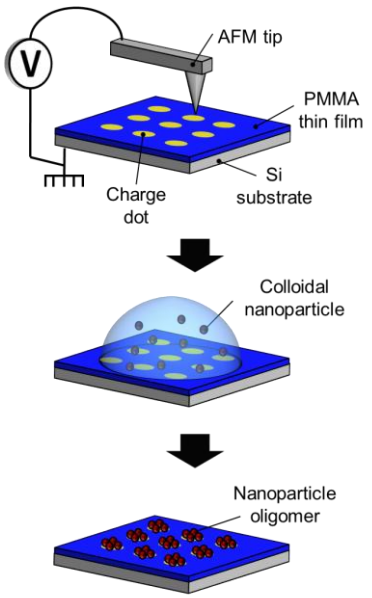

Fig. 1 Schematics of AFM nanoxerography: AFM charge writing (top), development by incubation of the colloidal suspension on the charge patterns (middle), and resulting nanoparticle oligomer array (bottom).

SERS measurements

SERS measurements were performed on a WITec system, using 633 nm and 785 nm laser excitation sources. By combining optical microscopy and AFM imaging on the same microscope, the area of interest can be easily located and scanned, and Raman spectra could be recorded at each pixel of an array. Integration times/ pixel of 0.1-0.25 s were used, a 100x magnification air objective, and laser powers of 0.1-0.4mW at the microscope entrance. Cresyl Violet (CV) molecules were adsorbed on the NP arrays by dropcasting 10^{-5}M methanol solutions (2-3 µl) and drying by a gentle blow of air, prior to measurements.

SEF measurements

Fluorescence measurements were performed on a MicroTime200 time-resolved confocal fluorescence microscope system, from PicoQuant, equipped with a picosecond diode laser head operating at 510 nm/40MHz (LDH-D-C-510, Pico-Quant) and a 100x/NA=0.9 magnification air objective (diffraction-limited spot size of 350 nm). The signal collected through the objective was spatially and spectrally filtered by a 50 µm pinhole and a FF01-519LP (Semrock, New York, USA) emission filter, respectively, before being focused on a PDM Single Photon Avalanche Diode (SPAD) from MPD. The detector signals were processed by the PicoHarp 300 Time-Correlated Single Photon Counting (TCSPC) data acquisition unit. Fluorescence spectra and lifetime decays were simultaneously obtained at room temperature by using a SR-163 spectrograph equipped with a Newton 970 EMCCD camera from Andor Technology coupled to an exit port of the main optical unit of MicroTime200 through a 50 µm optical fibre. A 50/50 beamsplitter was used to split the signal from the analyzed point towards the spectrograph and TCSPC unit of the MicroTime200 system. The oligomer arrays were first observed by optical microscopy, followed by a fluorescence lifetime imaging (FLIM) scan, in order to identify the areas of interest. A

Cite this: DOI: 10.1039/c0xx00000x

www.rsc.org/xxxxxx

ARTICLE TYPE

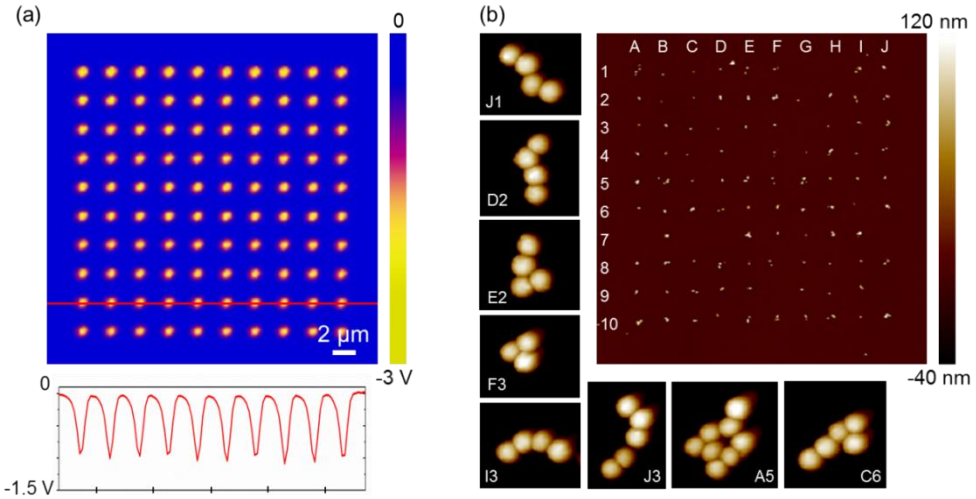

Fig. 2 Example of a directed assembly of Au@SiO_2@Rhodamine NPs into an array of 10×10 oligomers by AFM nanoxerography: (a) KFM image of 10×10 negatively charged dots written by AFM on a 100nm thick PMMA film, using -45 V voltage pulses. The surface potential profile of the line of charge dots marked by the red line on the KFM image is shown at the bottom, (b) AFM image of the resulting Au@SiO_2@Rhodamine nanoparticle oligomer array, using a colloidal suspension of concentration C_0= 6 x 10^{10} NPs/mL. Also shown are the high-resolution AFM images of selected oligomers.

small region (100×100 pixel images, pixel size below 100 nm), was selected including the investigated NP oligomer, which was then placed into the centre of the excitation focus for recording fluorescence lifetime and collecting the fluorescence spectra.

FDTD simulations

The local densities of states (LDOS) of the various plasmonic arrangements have been simulated by solving Maxwell equations using the three dimensional finite-difference time-domain (FDTD) method, as implemented in the freely available MEEP software package.[47] They were obtained by i) Fourier transforming the response to a short, broadband, point dipole (electric current) Gaussian pulse located in the centre of the structure and polarized along the substrate and ii) normalizing this response with the one obtained for a point dipole located at the same distance from the substrate under the same excitation conditions. In these simulations, perfectly matched layers were implemented in all directions. The dielectric permittivities of the glass substrate and silica were taken as 2.3 and 2.1, respectively. The dielectric permittivity of gold was specified by using a sum of Drude and Drude-Lorentz terms, according to the work performed by Rakic *et al*.[48] For SERS simulations, the size of the NPs in the oligomers was determined from AFM analyses. For SEF simulations, the size of the core-shell particles was determined from AFM analyses, while the core itself was supposed to be 50 nm in diameter. The positions of the NPs within an oligomer were determined by AFM. Details on the procedure for calculating the photonic local density of states ($D(\omega)$), the far-field radiated power($P_l^r(\omega)$) and Purcell factors (F) are given in the ESI.

Results and discussion

To enhance the emission of secondary radiation (SERS or SEF) $I(\omega')$ by a quantum system, one may enhance the incident photon density at frequency ω, $I_0(\omega)$, at the position of the emitter in question, which constitutes a real field concentration by the local field enhancement factor. Alternatively, one may increase the density of photon states at the frequency of secondary radiation ω', $D(\omega')$, a vacuum field concentration. Therefore, $I(\omega')=I_0(\omega)$*[interaction term]*$\times D(\omega')$, where the interaction term has to be appropriately defined for each process (SERS or SEF), and is notably responsible for the so-called chemical enhancement factor in SERS.[25,49] The enhancement of the photon LDOS, pioneered by E. M. Purcell, can be interpreted as the development of a certain Q-factor (ratio of energy accumulated in the system to the portion of energy the system loses in a single oscillation period) in a spatial domain where a test emitter (atom or other quantum system) is placed. Hot spots thus are local (near-field) zones in plasmonic nanostructures where high Q-factors can develop both at the incident and emitted (or scattered) light frequencies. To explain huge enhancement factors exceeding 10^{10} in SERS, enhancements of incident and emitted fields are typically discussed to arrive at a hypothetical enhancement factor:

$$F = \frac{|E(r,\omega)|^2|E(r,\omega')|^2}{|E_0(\omega)|^2|E_0(\omega')|^2} \approx \frac{|E(r,\omega)|^4}{|E_0(\omega)|^4}, \quad (1)$$

instead of the correct one: $F = \frac{|E(r,\omega)|^2 D(r,\omega')}{|E_0(\omega)|^2 D(\omega')}$.[49,50] (2)

Cite this: DOI: 10.1039/c0xx00000x

www.rsc.org/xxxxxx

ARTICLE TYPE

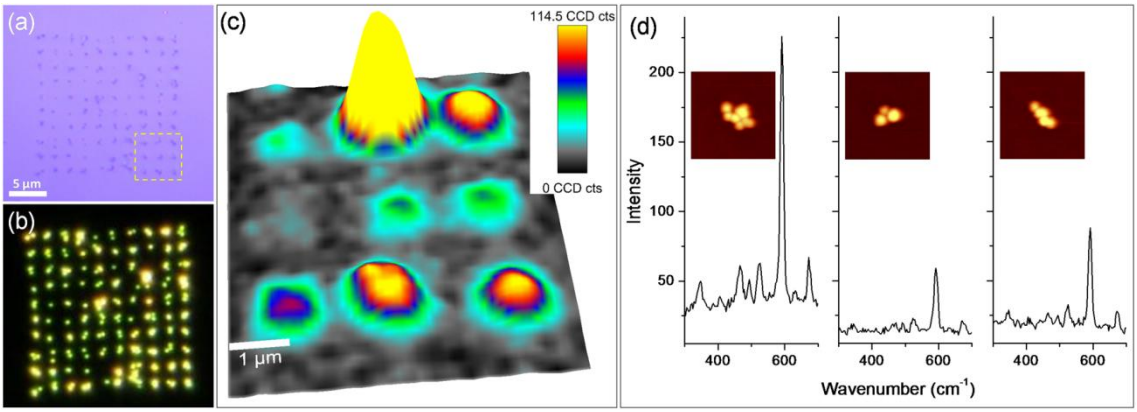

Fig. 3 (a) Bright-field and (b) dark-field optical microscopy images of an array of 10×10Au@TDSP NP oligomers assembled on charge dots written with +60 V voltage pulses, using a colloidal suspension of concentration C_0= 6 x 10^{10} NPs/mL. (c) SERS image of the area marked in a), constructed from the Cresyl Violet 589 cm^{-1} SERS band intensity; (d) selection of SERS spectra with corresponding sites in the inset.Caption

One of the purposes of this paper is to investigate the secondary radiation processes in gold NP oligomers (clusters made of a small number of particles) and to analyze the results obtained in the framework of the LDOS effect.

Assembling NPs into oligomer arrays by AFM nanoxerography

The specifically designed Au@TDSP and Au@SiO_2@Rhodamine NPs were assembled into arrays of oligomers as described in the Experimental section (Figure 1). Figure 2 presents a typical example of directed assembly of 90 nm Au@SiO_2@Rhodamine NPs into oligomers by AFM nanoxerography. The KFM image in Figure 2a shows an array of 10 × 10 negatively charged dots separated by 2.5 µm, written in a PMMA thin film with voltage pulses of -45 V. As shown on the profile, the surface potential of the charge dots is -1.15 V, with a full width at half maximum (FWHM) of around 700 nm, for the specific conditions used. The AFM topographical images presented in Figure 2b shows the resulting directed assembly of the Au@SiO_2@Rhodamine NPs into oligomers, upon using a colloidal suspension of concentration C_0= 6 x 10^{10} NPs/mL. Under these experimental conditions, 90% of the charge dots are covered by NP oligomers. The oligomeric clusters consist of 5±3 Au@SiO_2@Rhodamine nanoparticles each and present different orientational ordering or configurations. Similar Au@TDSP nanoparticle clusters were obtained on charge dots written with +60 V voltage pulses using a colloidal suspension of similar concentration (Figure 3a,b). Although the nanoxerography process offers a good control over the positions of the oligomers, e.g., in an array, the current state of development of this technique does not allow a perfect control over the number of NPs and their relative positioning with respect to each other, within the oligomer. However, the average number of NPs within the oligomers can be tuned by varying two key parameters: the surface potential of the charge dots through the amplitude of the voltage pulses used for AFM charge writing and/or the concentration of the colloidal suspensions.[39] High surface potentials of the charge dots and high concentration of the colloidal suspension favour the formation of larger clusters. The arrays of NP oligomers can be readily located by standard optical microscopy, both in bright-field and dark-field visualization modes, as demonstrated by the AFM images displayed in Figure 3a,b. The desired area and each specific oligomer can thus be readily addressed by the focused laser beam used for SERS or SEF excitation.

Polarized SERS experiments

The three-dimensional colourmap in Figure 3c represents an example of SERS image of a region containing 3×3 Au@TDSP NP oligomers marked by a rectangle in Figure 3a. The image was obtained by plotting the intensity of the Cresyl Violet (CV) band at 589 cm^{-1}. Since the configuration of each NP oligomer is known from AFM analyses, the dependence of SERS efficiency on the particular size and geometry of a given oligomer can be analyzed. Figure 3d presents a selection of SERS spectra of adsorbed CV molecules, collected from the NP oligomers shown in the insets. As a main tendency, the larger clusters, containing more interparticle gaps exhibit higher enhancements. The observed intensities and positions of CV SERS bands are in good agreement with previous reports;[51] the most intense band, at 589 cm^{-1} is attributed to a combination of ring modes, according to the literature.[51] In all measured spectra this band was the most intense, while additional weaker bands at, *e.g.*,465cm^{-1} and 673 cm^{-1}, can also be observed. Note that the 520 cm^{-1} band is attributed to the underlying Si substrate.

In the following, results of polarized SERS measurements on two selected oligomers (a trimer and a pentamer) with interesting configurations are discussed. Figures4 and 5 summarize the polarized SERS behaviour of the selected NP trimer and

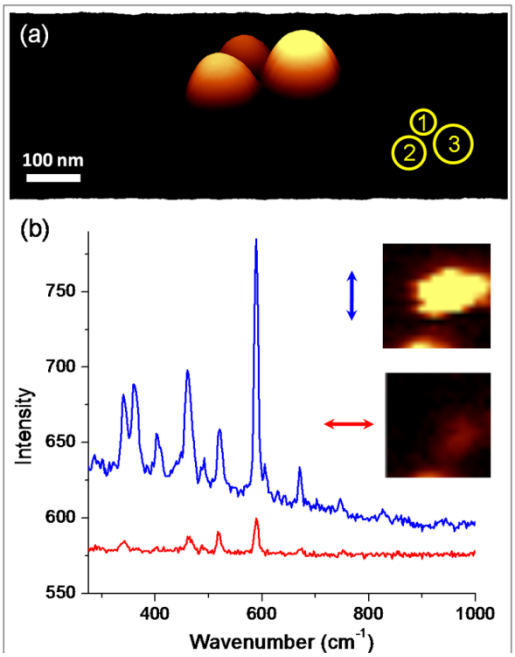

Fig. 4 (a) AFM 3D image of a NP trimer; inset schematizes the structure used for FDTD simulations. (b) SERS spectra and images (inset) of Cresyl Violet on this NP trimer, for the two incident polarizations indicated by arrows.

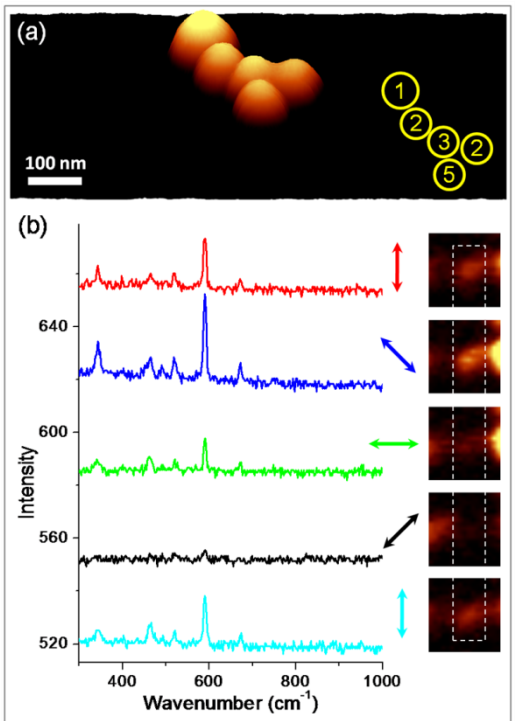

Fig. 5 (a) AFM 3D image of a Au@TDSP NP pentamer; inset schematizes the structure used for FDTD simulations; (b) SERS spectra and images (inset) of Cresyl Violet on this NP pentamer, for the incident polarizations indicated by arrows.

pentamer, respectively. The first observation is that the SERS intensity is strongly dependent on the polarization of the excitation beam. In the case of the trimer, for the most intense band at 589 cm^{-1}, the ratio between the SERS intensity corresponding to the incident vertical polarized light I^V and that of the horizontal one I^H (see Figure 4) is about 7. To verify the stability of the SERS signal, after performing the horizontal and the vertical polarization scans in this order, the horizontal configuration was re-recorded; the result was remarkably similar with the initial one (see ESI), ensuring the consistency of our results. As already established in many published reports, the local field enhancement induced by gap plasmons is critically dependent on the gap size and orientation of the incident polarization with respect to the gap axis.[30,52] Therefore, the observed behaviour can be explained by considering two factors: (i) the gap between particles 1 and 2 is smaller than the gap between particles 1 and 3 (particle 2 and 3 are clearly far from each other), and therefore produces the largest enhancement; (ii) the gap between particles 1 and 2 is more vertically oriented than the gap between 1 and 3. Further, it is worth analyzing the I^V/I^H ratio for different SERS bands. For the bands at 341, 465, 589, and 670 cm^{-1} this ratio is 7.15, 6.72, 7.41, and 6.23, respectively. Note that, excepting the 589 cm^{-1} band, the ratio decreases as function of wavenumber. This trend also correlates with the differences in the magnitude and slope of the SERS backgrounds for the vertical and horizontal polarizations. On a wavelength scale, the difference between the 341 cm^{-1} and 670 cm^{-1} SERS bands is about 22 nm, an amount that can matter when considering the relative width of the oligomers' plasmon resonances. The behaviour followed by both the enhancement of SERS bands and background, could thus be explained by different spectral profiles of the plasmon resonances excited by each polarization. This is in agreement with previous results demonstrating that the profile of the SERS spectrum can follow the profile of the overlapping plasmon resonances.[22] It is premature to explain the exception of the most intense band at 589 cm^{-1} from this trend. Probably, as different sets of molecules are actually probed at different locations (location of enhanced fields in each polarization) in the two configurations, some molecules could be differently oriented with respect to the metal surface, leading to a different degree of enhancement of different vibrational modes. This suggestion could be corroborated with the peculiar appearance of a SERS band at 360 cm^{-1}, which was not observed systematically throughout the experiments (see spectra in Figures 3 and 5). For the pentamer, the largest intensity signal was acquired for the 135° incident polarization (roughly oriented along the pentamer longest axis), and is about 8 times larger than the least intense signal acquired for the 45° polarization (Figure 5). A change of band intensity ratio was also observed for the NP pentamer analyzed here. However, the behaviour is not so prominent, and the most striking effect on the pentamer remains the difference in the intensities for the different polarizations.

A strong dependence of the SERS signal on the polarization of the excitation beam was observed for several oligomers of different geometries. A modification of the SERS bands relative intensity ratio was also observed, which correlates with the background spectrum, and possibly with the underlying plasmonic profile. This behaviour is in agreement with previous results on ordered arrays of elongated nanoparticles made by electron lithography.[22] Our results confirm that the behaviour is valid also for chemically synthesized NP oligomers, highlighting

the general nature of such effects.

SERS simulations

In order to understand the origin of these polarization effects on the signal enhancement, we performed FDTD simulations based on the LDOS approach, as described previously and in the ESI. Notably, in Raman scattering, if one neglects the local field effect responsible for the excitation enhancement and considers only the influence of polarization on the emission field, one expects the enhancement to scale as:

$$\frac{D(r,\omega')}{D(\omega')}. \quad (3)$$

In the calculations, the Raman spectrum $RS(\omega')$ was firstly constructed as a sum of Gaussian Peaks with a standard deviation of 5 cm^{-1} and centred on 340, 400, 470, 490, 590, 680 and 750 cm^{-1}, with relative amplitudes of 2, 1, 2, 0.5, 4, 1, 0.5, respectively. In a second step, we determined the LDOS $D_l(r,\omega')$ of emitters located at well-defined positions, with well-defined orientations of the dipoles in the oligomeric structures.We proceeded, in exactly the same excitation conditions, for emitters located on top of the glass substrate, taken as a reference and obtained $D_l(\omega')$.

Finally, we calculated the enhanced Raman spectrum as:

$$RS(\omega') * \frac{D_l(r,\omega')}{D_l(\omega')}. \quad (4)$$

The results of this approach are illustrated in Figure 6. Clearly, such calculations fully reproduce the observed experimental behaviour. The simulated spectra displayed in Figure 6a for the trimer shows an enhanced Raman signal for the vertical incident polarization, which is 7 to 40 times larger than that for the horizontal polarization. It also shows that not only polarization matters, but the position of the emitter (Raman reporter) also plays an important role. In Figure 6a, the solid lines pertain to an emitter located in the centre between particles 1 and 2 (see inset). These two particles are very close to each other, giving an enhancement in the vertical polarization 40 times larger than in the horizontal polarization. On the contrary, the dashed lines pertain to an emitter located at the centre of the gap between particles 1 and 3. The gap between these two particles is bit larger than between particles 1 and 2. Accordingly, the enhancement is less spectacular. As the orientation of this dimer is closer to horizontal, the enhancement is now maximal for the horizontal polarization, and is only 4 times larger than that in the vertical polarization. Considering both locations of the emitters, giving a maximum enhancement as light is polarized either in the vertical direction (solid blue line) or in the horizontal position (dashed red line), the relative enhancement between vertically and horizontally polarized emitters in the trimer is 7, *i.e.* very close to the observed experimental enhancement. The geometry of this trimer, with particle 1 smaller than the other two particles (see inset in Figure 6a) is reminiscent of a structure proposed by Li *et al.*,[53] for which a 'nanolens' effect develops the nanofocus effect (hottest spot) in the gap between the smallest nanospheres, where the local fields are enhanced.

By estimating the ratio I^V/I^H for the bands at 341, 465, 589, and 670 cm^{-1} this ratio is 7.34, 7.18, 7.07, and 7.01 respectively. Although the differences are not spectacular, they clearly

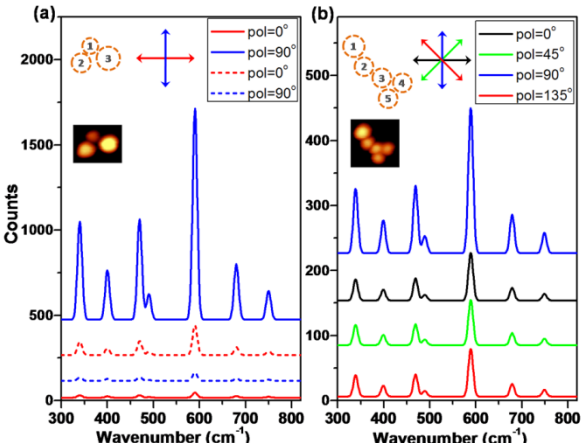

Fig. 6 Simulated enhanced Raman spectra of: (a) the Au@TDSP NP trimer, for the two indicated incident polarizations, with the emitter located in the gap between particles 1 and 2 (solid lines), and between particles 1 and 3 (dash lines); (b) the Au@TDSP pentamer, for multiple polarizations as indicated, with the emitter located in the gap between particles 3 and 4.

replicate the trend observed in the experiments, the ratio decreasing as the wavenumber increases.

Concerning the semi-elongated pentamer, results indicated that both the dipole orientation and spatial location of the emitter in the structure play an important role in the enhancement effect. The situation where an emitter is located in the gap between particles 3 and 4 (inset in Figure 6b), which has shown the maximum calculated enhancement, is displayed in Figure6b. In this case, the enhanced signal for a vertically polarized incident beam is larger than for any other excitation polarization (i.e. 0°, 45°, 135°) by a ratio of 3.

These simulations confirm the important role played by the orientation of the polarization with respect to the interparticle gap axis. They also show that the enhancement experienced by a Raman scatterer is strongly affected by its location within the oligomer. Thus, the experimental results obtained can be interpreted mainly as being strongly determined by the relation between the incident laser polarization and the oligomer geometry. It is also important to emphasize that the FDTD simulations based on the LDOS approach pretty well reproduce experimental results, even for fine details such as the modification of the relative band intensity. As the LDOS probes the plasmonic modes at the emission frequency, our simulations support an interpretation of SERS enhancements beyond the E^4 approximation.[22]

SEF experiments

We performed fluorescence confocal microscopy on individual Au@SiO_2@Rhodamine B NP oligomers containing varying number of NPs and interparticle orientations. This was done in order to determine the influence of the various enhancement factors on the emission spectra and spontaneous decay rates of the fluorescence emitters grafted on the surface of Au@SiO_2 NPs.

Figure 7 shows the normalized fluorescence decay profiles recorded for various specific geometries of the NP oligomers, varying from a single monomer (a) to dimers (b), trimers (c), tetramers (d), pentamers (e) and higher order multimers (f). For a

Cite this: DOI: 10.1039/c0xx00000x

www.rsc.org/xxxxxx

ARTICLE TYPE

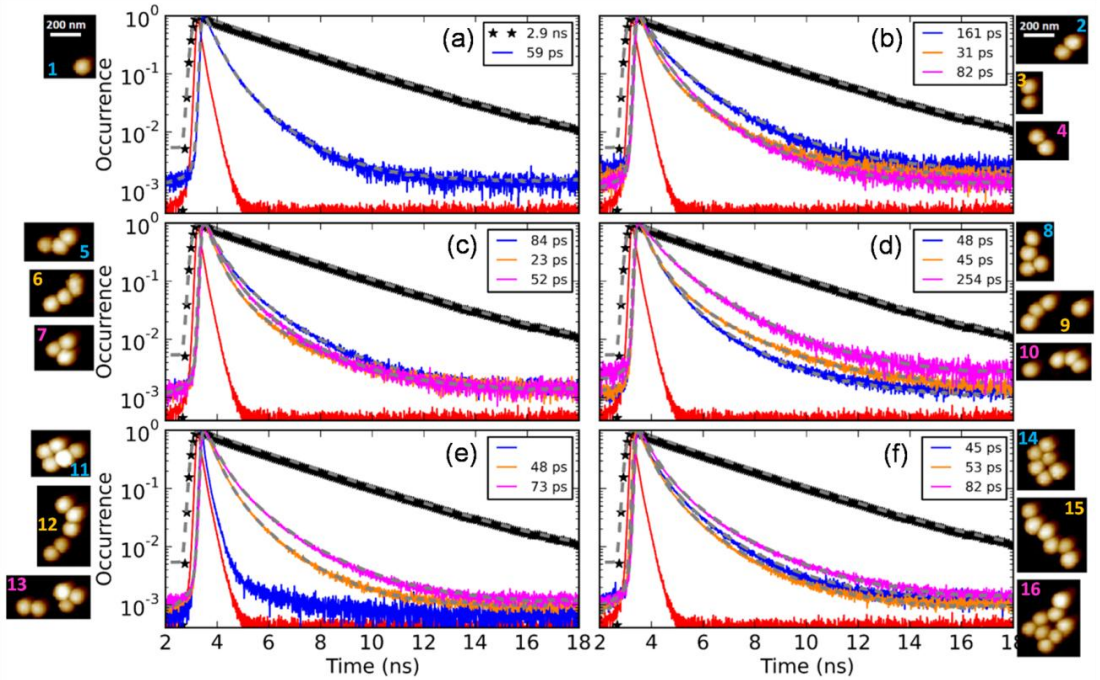

Fig. 7 Fluorescence decay curves of Rhodamine B on the Au@SiO_2@Rhodamine B NP oligomers shown in the AFM images next to each panel. The black curve corresponds to isolated Rhodamine B molecules in solution. Values of the estimated decay times are given in the legends. For each panel, the AFM images and legend information are correlated by their vertical positions and colour code.

given panel, the correlation between the AFM images and the curves on the graph is given by both the vertical position and colours of the numbering. On each panel, the decay profile of Rhodamine B molecules dispersed in a 10^{-6} M (in order to avoid aggregation) ethanol solution is shown for comparison (black curve). Let us note immediately that the typical single exponential decay profile observed for Rhodamine B in solution is not recovered from Au@SiO_2@Rhodamine B NP oligomers. Although the core-shell particles synthesized in this study are well controlled in size, shape and the spacing (~20 nm) between the dye molecules and the Au core surface, i) the NPs are never perfectly spherical, ii) the silica shell acting as a spacer presents typical roughness and is not uniformly thick (see Figure SI-2, ESI), and iii) the orientation of the molecules with respect to the Au core surface is currently impossible to control experimentally. These factors make i) the surface plasmon resonance shifting in frequency and ii) the strength of the dipole-dipole interaction between the molecules and the Au cores changing from one NP to another. These factors clearly explain the origin of the non-exponential decay profiles.

Another significant feature exhibited in Figure 7 is the expected significant shortening of the decay times once the emitters experience the proximity of the metallic cores instead of being isolated in ethanol. At least a 10-fold shortening (that can possibly reach a 100-fold) is observed depending on the specific geometry of the oligomers, induced by the modified LDOS around the plasmon resonance. In order to appropriately fit such decay profiles, we used a stretched exponential function:

$$I(t) = I_0 \exp[-(\frac{t}{\tau_K})^{\beta}], \quad (5)$$

by introducing a stretching parameter $0<\beta<1$ in the logarithmic time, featuring a whole distribution of decay times, convoluted with the instrumental response function (IRF, red curve in each panel). The decay time (mean relaxation time) is then obtained from the relation:

$$< \tau >= \frac{\tau_K}{\beta}\Gamma(\frac{1}{\beta}), \quad (6)$$

where Γ is the gamma function. For $\beta = 1$, the exponential decay with $\tau = \tau_K$ is recovered and, as β strongly departs from 1, more exponential relaxations are involved in the superposition. In Figure7, these fits appear as grey dashed lines superimposed on the experimental data. The adequacy of the fits is clearly noticed, and the mean decay times indicated in the legends of Figure7 are estimated within 10 % accuracy, based on the covariance matrix of the performed least square analysis. The determined decay rates Γ obviously include a radiative and a non-radiative part, as:

$$\frac{1}{<\tau>} = \Gamma = \Gamma_r + \Gamma_{nr}, \quad (7)$$

the latter being essentially due to Ohmic losses in the Au cores. Depending on the geometry, for oligomers consisting of the same

Cite this: DOI: 10.1039/c0xx00000x

www.rsc.org/xxxxxx

ARTICLE TYPE

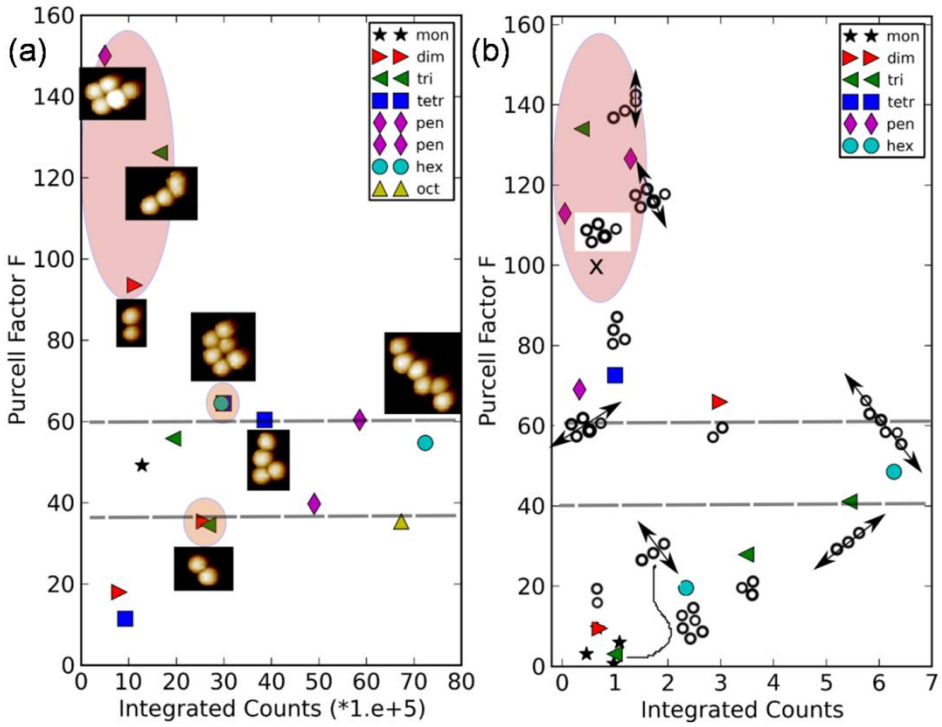

Fig. 8 Correlation plot between the Purcell factor and integrated emission intensity obtained by experiment (a) and simulations (b) on different Au@SiO_2@RhodamineB NP oligomers.

number of NPs, decay times varying by a factor larger than 5 may be observed, as demonstrated for two very similar dimers (Figure 7b) and likewise for two very similar tetramers (Figure 7d). A pentamer (no.11 in Figure 7e) exhibited such a short decay profile that it could not be fitted reliably. Moreover, this pentamer does not deliver enough radiative emission counts. The exact geometry of the oligomers and the competition between the radiative and non-radiative decay channels at the position and orientation adopted by the molecules thus largely determine the radiative efficiency.

Figure 8a shows a correlation plot between the Purcell factor, determined experimentally as:

$$F = \frac{\Gamma}{\Gamma_0} \qquad (8)$$

(Γ is the total decay rate of the emitters grafted to a specific oligomeric geometry and Γ_0 is the total decay rate of the emitters in ethanol), and the total number of counts delivered by the structure. The trend exhibited by the correlation plot is not very clear: the plot is neither correlated nor anti-correlated. Nevertheless, it is not a random cloud of points either. Two lines seem to increase prior to reaching a saturation level at about F=40 and F=60. Furthermore, the ellipse drawn in top-left corner of Figure 8a comprises three points for which the number of counts is minimum for a maximum Purcell factor. Here, the non-radiative part of the Purcell factor seems to play a major role. Finally, the two drawn circular zones each enclose two points exhibiting approximately the same number of counts for the same Purcell factor, for different oligomeric arrangements. The first such zone is in the saturation zone of the Purcell factor F=40 and involves a dimer and a trimer. The second is in the saturation zone F=60 and involves a packed hexamer and a tetramer. As these zones further correspond to a minimum integrated number of counts for the given F saturation level, these oligomers maximize the number of their non-radiative decay channels. On the contrary, an extended hexamer (no.15 in Figure 7) exhibits the largest recorded number of counts at the same plateau value F=60 as the packed hexamer (no.14 in Figure 7). For statistically the same number of molecules grafted on the packed and extended hexamers, the latter thus maximizes the radiative emission.

We measured the fluorescence spectra simultaneously with the decay rates, owing to the 50/50 beam-splitter introduced in the detection path. Such an observable provides exquisite information about the exact frequency range in which the surface plasmon enhancement of the oligomer takes place, whether its effect manifests in the form of the local-field or LDOS enhancements. Figure 9 shows the normalized (with respect to the maximum, indicated in the inset) fluorescence spectra of the oligomeric arrangements corresponding to the decay profiles of Figure 7.

Cite this: DOI: 10.1039/c0xx00000x

www.rsc.org/xxxxxx

ARTICLE TYPE

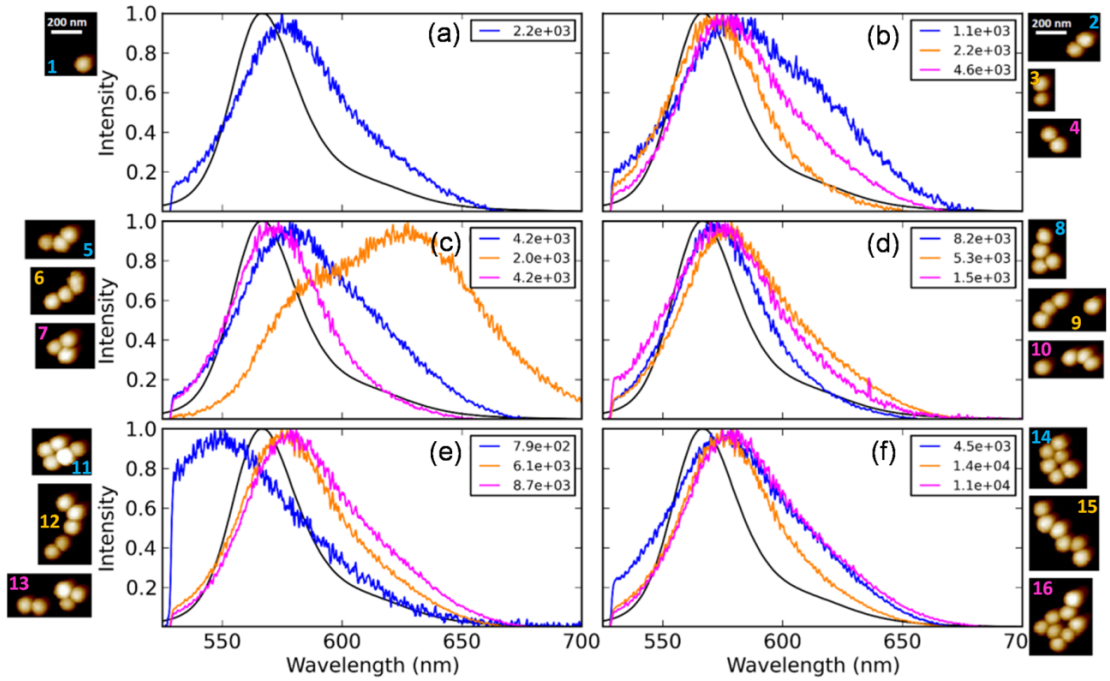

Fig. 9 Emission spectra (normalized) of the Au@SiO_2@Rhodamine B NP oligomers shown in the AFM images next to each panel. The black curve corresponds to the emission of isolated Rhodamine B molecules in solution. Values of the maximum emission intensity are given in the legend. Note that these spectra correspond to the decay curves in Figure 7. For each panel, the AFM images and legend information are correlated by their vertical positions and colour code.

Most spectra are red-shifted (to different extents), with respect to the spectrum of isolated Rhodamine B molecules in solution.

On an average, one might reasonably assume that as the number of NPs constituting the considered oligomers increases (from Figure 9a to 9f), so does the number of grafted molecules per oligomer and thus the number of counts delivered by this oligomera behaviour consistent with radiative emission. A notable exception to the last two statements is the blue shifting of the spectrum of pentamer no.11 in Figure 9e concomitant with a low value of its maximum intensity. This pentamer also exhibits a very short decay time (Fig. 7e), which, in terms of spontaneous emission rate can be either due to a large radiative decay rate or a large non-radiative decay rate (see eq.7). As the emission intensity of this oligomer is very low, undoubtedly this particular pentamer favours non-radiative losses. Together with the long wavelength shift exhibited by most spectra, one often observes an enhancement of the vibronic shoulder of Rhodamine B. This vibronic shoulder enhancement can also be drastically different for the same type of oligomer. Dimer no.2 shown in Figure 9b for example, which exhibited a 5 times lower decay rate enhancement (Figure 7b) than dimer no.3, develops a significant vibronic peak. It appears that, for some reason, more energy is dissipated in vibrational motion instead of radiative emission in dimer no.2 as compared to the no.3, a process very favourable to SERS observation. Even more significantly, an extended trimer (no.6) in Figure 9c exhibits a huge vibronic shoulder as compared to the one shown by the triangular trimer (no.7). In this case, the decay rate of the extended trimer was more than twice as large as that of the triangular trimer (Figure 7c), which makes the previous argument difficult to sustain: this extended trimer distributes more radiative energy and vibrational dissipation than the triangular trimer, *i.e.* a situation favourable to both SERS and SEF.

As such, we showed in this section that, depending on the oligomer geometry, a 10 to 100-fold shortening of fluorescence decay times is observed. Most spectra are red-shifted (to different extents), with respect to the spectrum of isolated Rhodamine B molecules in solution. Also, the dependence of the Purcell factor on integrated emission intensity shows an interesting behaviour: given saturation levels are observed around F=40 and F=60. It is not completely clear up to now, why such plateau occur and what is the exact role of the oligomer's geometry on the distribution of energy in radiative and non radiative channels.

SEF simulations

The experimental geometries of the NP oligomers obtained by AFM (see Figures 7 and 9) have been used to generate the numerical arrangements, so that the relative position and size of each core-shell particle constituting a given oligomer are precisely set. Although the Au core diameter varies slightly from

Cite this: DOI: 10.1039/c0xx00000x

www.rsc.org/xxxxxx

ARTICLE TYPE

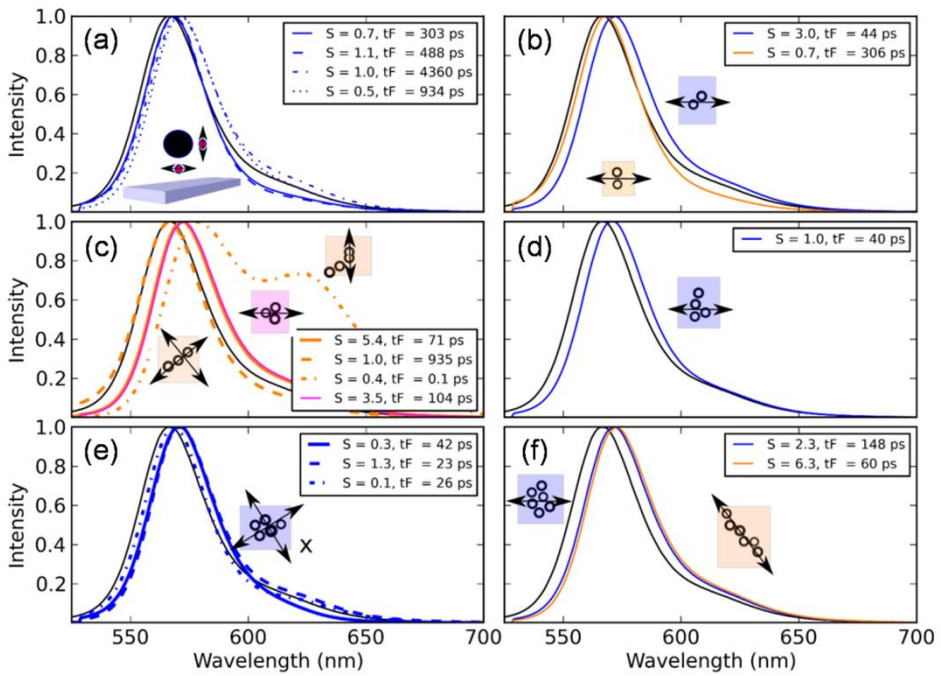

Fig. 10 Simulated emission spectra (normalized) for the indicated oligomer configurations. Insets report values of the total integrated spectrum and decay time.

particle to particle (TEM images in Figure SI-2), one cannot distinguish them by AFM. Hence, this parameter has been set uniformly at 50 nm. In all cases, a single impulsive dipole current source (emitter) was used, with its position centred at best in the oligomer, taking care that it indeed resides at the surface of a core-shell particle. At first, the orientation of the dipole has been taken along *x*-axis in all simulations. In a second step, we proceeded to some polarization refinement in order to obtain a better agreement with the experimental results.

Figure 10 shows the obtained simulated spectra $S(\omega)$ (see ESI for the procedure) for some monomers (a), dimers (b), trimers (c), tetramer (d), pentamer (e) and hexamers (f). In the legend of each panel are indicated the values of the total integrated spectrum:

$$S = \int_0^\infty S(\omega)d\omega \qquad (9)$$

and decay time t_F of the single emitter, for each polarization indicated by a double arrow drawn on the specific considered oligomer. These values are collected in Figure 8b, for the sake of comparison with experiments (Figure 8a). Figure 10 clearly shows that all oligomeric spectra are red-shifted, similar to what was observed in the experiments. The overall agreement between simulated and experimentally (Figure 9) recorded spectra is generally good, with a few exceptions. The calculated decay times t_F (and Purcell factors F) match reasonably well with those obtained from experiments (Figure 7).

Let us recall first that the oligomers in the experiments were situated on a substrate. This substrate was also taken into account in the simulation. Considering the monomer (Figure 10a), we envisaged 4 different polarization conditions. We assumed the emitter to be located either i) on the side of the particle, *i.e.* 50 nm away from the substrate and polarized either normally or tangentially to the particle or ii) at the interface between the substrate and the particle with its polarization either tangential or normal to the particle. Case (ii) clearly provides spectra that are more red-shifted than case (i). However, the latter case provides the largest decay times, possibly exceeding the decay time of an isolated emitter in the case where it is located at the interface and polarized tangentially to the sphere (and parallel to the substrate). The corresponding experimental spectrum (Figure9a) and decay time (Figure 7a) undoubtedly results from the superposition of the responses provided by the single emitters involved in cases (i) and (ii) and many more configurations.

In the case of the dimers (Figure 10b), the red-shifting of the spectra is more pronounced in the oblique-oriented dimer than in the vertical dimer, in accordance with the experiments (dimers no.2 and no.3 in Figure 9b), with the emitter dipole in the *x*-direction. However, their respective decay times and integrated intensities do not evolve exactly as in the experiment. Many more configurations of the polarizations and locations of the emitters are needed to reproduce the experimental data.

The packed and extended hexamers shown in Figure 10f have been excited with a polarization along *x*-axis (horizontal) and along the oligomeric "chain" axis, respectively, as seen in the

insets. Their spectra are both equivalently red-shifted with respect to the case of the isolated molecule and show integrated intensities that evolve in a way similar to the experiments (oligomers no.14 and no.15 in Figures 9f and 7f). However, the packed hexamer exhibits a decay time numerically larger than that estimated experimentally. For the extended hexamer, the numerical and experimental decay times are in very good agreement. Figure 8 further exemplifies this difference. Although experimentally both hexamers have a similar Purcell Factor $F \sim 60$, the packed hexamer is much below this line with $F \sim 20$ and the extended hexamer has a F value which closely reaches this line, both hexamers displaying a relative position of their integrated counts which nicely matches the experiment. Clearly, in the packed hexamer, the *x*-polarization of the emitter(s) has not been chosen experimentally, while a polarization along the main direction of the extended oligomer has certainly been selected.

The behaviour shown by the tetramer in Figure 10d embodies at once the experimental configuration of oligomer no.8. Indeed, for a single *x*-polarized emitter centred on the structure, the spectrum exhibits a red-shift comparable to the experimental one (Figure 9d) and the decay time t_F almost exactly matches the experimental value (Figure 7d). The correlation plots of Figure8 clearly show the good matching between the experimental and numerical situations for this tetramer with a Purcell factor $F \sim 60$, and 70, respectively.

The last two arrangements considered were subjected to considerable refinement in order to better match experimental results. The packed pentamer of Figure 10e, which experimentally exhibits a strong blue-shift of its spectrum (oligomer no.11 in Figure 9e) and a drastic shortening of its decay time (Figure 7e), was excited by a single emitter in three different orthogonal polarizations. It has been excited with i) the polarization in the plane and parallel to the longest side of the structure (inset in Figure 10e), ii) the polarization in the plane and perpendicular to the longest side of the structure and iii) the polarization out of the plane of the structure. Unfortunately, we could not recover the blue-shift of the spectrum with either of these polarizations. Nevertheless, cases (ii) and (iii) provided very short values of the decay times and integrated intensities compatible with the experiment. This is better seen in Figure8, in which the (S, F) coordinates of the experimental and numerical points for this oligomer belong to the same region on the graphs. On the other side, the extended trimer shown in Figure 10c, which presents a huge vibronic peak ~ 630 nm (oligomer no.6 in Figure 9c) and a very short decay time (Figure 7c) has been simulated with polarizations along and perpendicular to its main axis. As none of these polarizations provided either the large vibronic peak or the decay times and integrated intensities compatible with experiments, we carefully reconsidered the geometry of this oligomer and questioned the nature of the particle at the upper right end of the structure. Instead of a single particle this may very well be a small dimer that would not have followed the regular path of the synthesis, resulting in a dimeric species formed by two Au cores that were only partially coated by silica. To investigate this possibility, we numerically constructed such a hypothetical geometry, where the top-right particle is replaced by a small dimer, constituted by two Au core particles separated only by 10 nm from each other, due to a supposed incomplete silica shell formation and possessing a single emitter at the centre, oriented along the axis of this dimer. Figure 10c shows this simulated structure, which very much resembles the corresponding AFM image in Figure 7c (oligomer no.6) together with its spectrum, integrated counts and decay time. With this geometry and excitation conditions, we were able to reproduce the vibronic peak, in agreement with a reported study on the interaction of particles in a dimer.[54] Furthermore, the integrated intensity and Purcell factors match qualitatively with the experiments as shown in Figure 8, where this structure appears both experimentally and numerically in the same region of the graph (note that in this figure, the Purcell Factor has been significantly reduced to fit in the graph, compared with the value reported in Figure 9c). Finally, let us note here that the plateaus at $F \sim 40$, $F \sim 60$ observed experimentally on the correlation plot in Figure8 are also noticed numerically, while only slightly shifted.

These LDOS-based simulations were able to satisfactorily reproduce many features observed in the experimental spectra, such as red-shift of the fluorescence emission spectra, decrease of the decay time, enhancement of emission intensity, emission rate enhancement, proving the robustness of the method. Further, these simulations allowed investigating the role played by many factors such as the geometry of the plasmonic oligomer, polarization, the position of the emitter within the oligomer. Corroborated with the experimental observations, these support a SEF mechanism intimately connected to dipole-dipole and higher multipole-dipole interactions between the plasmon resonances of the oligomer and the emitters, respectively. The development and application of a framework taking these effects into account in complex geometries based on spherical particles could lead to new understandings in the plasmonics field.

Conclusions

Arrays of plasmonic oligomers made of either ligand protected Au or Au@SiO_2 core-shell colloidal nanoparticles were fabricated by AFM nanoxerography. AFM imaging allowed mapping the precise geometry/configuration of several NP oligomers. By confocal Raman/fluorescence microscopy, the SERS/SEF response of molecular Raman reporters/fluorophores adsorbed on the plasmonic oligomers was investigated. SERS studies on Au NP oligomers demonstrated a strong dependence of the SERS emission on the polarization of incident light relative to the specific geometry of the plasmonic oligomer. Moreover, we demonstrated by FDTD simulations on equivalent realistic structures, that a LDOS framework can reasonably predict such behaviour. The SEF studies, performed on a large collection of NP oligomers of various configurations showed interesting fluorophore decay rate modification and red-shift of the emission spectra. By employing a confocal FLIM microscope, fluorescence spectra and lifetime decays were simultaneously obtained for each individual oligomer, and these were correlated with the morphology of the oligomers. The experimental results were again well analyzed from a theoretical standpoint, within the LDOS framework. The polarization and location of the emitters have been shown to play an important role on the SEF properties. The saturation levels of the Purcell factor F observed both experimentally and numerically are intriguing features, which

clearly require further investigations. The proven potential of the LDOS approach as a very useful common tool for analyzing both SERS and SEF effects is one of the highlights of this work. The effect of the local density of states on emission properties could indeed be applied to SERS and SEF, which are both radiation processes. Raman scattering can be viewed as an absorption followed by an emission, just as fluorescence, with the specific condition that the excited state lifetime is much shorter, the process being nearly instantaneous. The LDOS therefore can play a decisive role on both Raman emitted (scattered) and fluorescence emitted photons. Since plasmon modes can strongly modulate the LDOS, the SERS/SEF photons can thus be also modulated through the LDOS. We hope that our results will encourage other joint studies of SERS and SEF, which should provide useful insights not only for SERS and SEF, but also for the field of plasmonics itself.

From the practical point of view, we anticipate that AFM nanoxerography could be further refined to better control the location of NPs within the oligomers, or the orientation of NPs possessing anisotropic shapes. Then, one could build oligomers made of NP colloids possessing simultaneously both SERS and SEF reporters.[55] We envisage such an approach in future studies, aiming at SERS/SEF analyses as those detailed in this paper, but performed on the same set of plasmonic oligomers.

Finally, we give some suggestions regarding the application potential of such oligomer arrays. Many kinds of SERS-based sensing schemes could be proposed, but a particular example which would exploit the morphology of these oligomer arrays is for multiplexed detection. By depositing mixtures of multiple analytes at very low concentrations over an oligomer array, one would expect that, statistically, the molecules are randomly adsorbed on the oligomers. Due to the low concentrations and the very low analysis volume (hot-spots within oligomers) one can then expect that the SERS spectrum recorded at a given oligomer would be dominated by one type of adsorbed analyte. Because each oligomer in an array can be addressed individually, by analyzing a collection of SERS spectra from many oligomers, e.g. by cluster analysis, the possibility opens to identify multiple analytes. Another possible application, exploiting the polarization sensitivity, is also high-security hidden barcodes/tags for counterfeiting control. For example with well-designed oligomers one could selectively read signals from molecules positioned at given specific locations within the NP oligomer. In turn, SEF effects in larger, chain-like plasmonic oligomers hold promise for plasmonic waveguiding/switching or lasing.

Acknowledgements

This work was supported by a grant of the Babes-Bolyai University, under the contract GTC_34057/2013.

Notes and references

[a]*Université de Toulouse, LPCNO, INSA-CNRS-UPS, 135 Avenue de Rangueil, Toulouse, 31077, France. Fax: +33561559697; Tel: +33561559645 E-mail:laurence.ressier@insa-toulouse.fr*

[b]*CNRS, University of Bordeaux, CRPP, UPR8641, 115 avenue Schweitzer, 33600 Pessac, France. Fax:3356845600; Tel: + 3356845612; E-mail: vallee@crpp-bordeaux.cnrs.fr*

[c]*Institute for Interdisciplinary Research in Bio-Nano-Sciences, Babes-Bolyai University, M. Kogalniceanu 1, 400084 Cluj-Napoca, Romania. Fax: 40264591906; Tel:40264454554; E-mail: cosmin.farcau@phys.ubbcluj.ro*

† Electronic Supplementary Information (ESI) available: optical extinction spectra, TEM images and size hystograms of the synthesized colloidal nanoparticles; details on the FDTD calculations of LDOS, Purcell factor, emission spectra; polarized SERS imaging. See DOI: 10.1039/b000000x/

1 B. Luk'yanchuk, N. I. Zheludev, S. A. Maier, N. J. Halas, P. Nordlander, H. Giessen, C. T. Chong, *Nat. Mater.*, 2010, **9**, 707.
2 D. E. Grupp, H. J. Lezec, T. W. Ebbesen, K. M. Pellerin, T. Thio, *Appl. Phys. Lett.*, 2000, **77**, 1569.
3 S. Zhang, D. A. Genov, Y. Wang, M. Liu, X. Zhang, *Phys. Rev. Lett.*, 2008, **101**, 047401.
4 H. Aouani, O. Mahboub, N. Bonod, E. Devaux, E. Popov, H. Rigneault, T. W. Ebbesen, J. Wenger, *Nano Lett.* 2011, **11**, 637.
5 R. F.Oulton,*Mater. Today*, 2012, **15**, 26.
6 A. G.Brolo,*Nat. Photonics*, 2012, **6**, 709.
7 X.-F. Zhang, M.-Q. Zou, X.-H. Qi, F. Liu, X.-H. Zhu, B.-H. Zhao, *J. Raman Spectrosc.*,2010, **41**, 1655.
8 K. Ataka, J. Heberle, *Anal. Bioanal. Chem.*, 2007, **388**, 47.
9 S. A. Elfeky, F. D'Hooge, L. Poncel, W. Chen, S. P. Perera, J. M. H. van den Elsen, T. D. James, A. T. A. Jenkins, P. J. Cameron, J. S. Fossey, *New J. Chem.* 2009, **33**, 1466.
10 E. Stratakis, E. Kymakis, *Mater. Today*, 2013, **16**, 133.
11 J. Dong, J. Liu, P. Liu, J. Liu, X. Zhao, G. Kang, J. Xie, Y. Wang, *Opt. Commun.*, 2013, **288**, 122.
12 Y. Hwang, H.-G. Park, *J. Opt.*, 2014, **16**, 025001.
13 E. C. Le Ru, Pablo G. Etchegoin, *Annu. Rev. Phys. Chem.*, 2012, **63**, 65.
14 H. M. Lee, S. M. Jin, H. M. Kimb, Y. D. Suh, *Phys. Chem. Chem. Phys.*, 2013, **15**, 5276.
15 T. Kang, S. M. Yoo, I. Yoon, S. Y. Lee, B. Kim, *Nano Lett.*, 2010, **10**, 1189.
16 Z. Zhou, H. Huang, Y. Chen, F. Liu, C. Zuang, N. Li, *Biosens. Bioelectron.*, 2014, **52**, 367.
17 H. Li, M. Wang, C. Wang, W. Li, W. Qiang, D. Xu, *Anal. Chem.*, 2013, **85**, 4492.
18 C.-Y. Shih, H.-C. Yeh, *Opt. Express*, 2012, **20**, 20698.
19 X. Gu, T. Qiu, W. Zhang, P. K. Chu, *Nanoscale Res. Lett.*, 2011, **6**, 199.
20 A. Kumar, R. Srivastava, D. S. Mehta, M. N. Kamalasanan, *Org. Electron.*, 2012, **13**, 1750.
21 B. Fazio, C. D'Andrea, F. Bonaccorso, A. Irrera, G. Calogero, C. Vasi, P. G. Gucciardi, M. Allegrini, A. Toma, D. Chiappe, C. Martella, F. Buatier de Mongeot, *ACS Nano*, 2011, **5**, 5945.
22 E. C. Le Ru, J. Grand, N. Félidj, J. Aubard, G. Lévi, A. Hohenau, J. R. Krenn, E. Blackie, P. G. Etchegoin, *J. Phys. Chem. C*, 2008, **112**, 8117.
23 T. H. Taminiau, F. D. Stefani, N. F. van Hulst, *New J. Phys.*, 2008, **10**, 105005.
24 H. Mertens, J. S. Biteen, H. A. Atwater, A. Polman, *Nano Lett.*, 2006, **6**, 2622.
25 S. V. Gaponenko, Introduction to Nanophotonics; Cambridge University Press: Cambridge, 2010.
26 L. Novotny, B.Hecht, Principles of Nano-Optics; Cambridge University Press: Cambridge, 2012.
27 E. Purcell, *Phys. Rev.*,1946, **69**, 681.
28 S. V. Gaponenko, *Phys. Rev. B*,2002, **65**, 140303.
29 M. Hentschel, D. Dregely, R. Vogelgesang, H. Giessen, N.Liu, *ACS Nano*, 2011, **5**, 2042.
30 J. Z. Zhang, C. Noguez, *Plasmonics*, 2008, **3**, 127.
31 C. Burda, X. Chen, R. Narayanan, M. A. El-Sayed, *Chem. Rev.* 2005, **105**, 1025.
32 P. Mesquida, A. Stemmer, *Adv. Mater.*, 2001, **13**, 1395.
33 S.-D. Tzeng, K.-J. Lin, J.-C. Hu, L.-J. Chen, S. Gwo, *Adv. Mater.*,2006, **18**, 1147.
34 L. Seemann, A. Stemmer, N. Naujoks, *Microelectron. Eng.*, 2007, **84**, 1423–1426.

35 L. Ressier, E. Palleau, C. Garcia, G. Viau, B. Viallet, *IEEE Trans. Nanotechnol.*, 2009, **8**, 487.
36 M. Beija, E. Palleau, S. Sistach, X. Zhao, L. Ressier, C. Mingotaud, M. Destarac, J.-D. Marty, *J. Mater. Chem.* 2010, **20**, 9433.
37 E. Palleau, N. M. Sangeetha, L. Ressier, *Nanotechnology*, 2011, **22**, 325603.
38 E. Palleau, N. M. Sangeetha, G. Viau, J.-D. Marty, L. Ressier, *ACS Nano*, 2011, **5**, 4228.
39 N. M. Sangeetha, P. Moutet, D. Lagarde, G. Sallen, B. Urbaszek, X. Marie, G. Viau, L. Ressier, *Nanoscale*, 2013, **5**, 9587.
40 S. Lemonier, P. Moutet, W. Moussa, M. Destarac, L. Ressier, J.-D. Marty, *Gold Bull*., 2013, **46**, 267.
41 C. Ziegler, A. Eychmüller, *J. Phys. Chem. C*, 2011, **115**, 4502.
42 N. M. Sangeetha, N. Decorde, B. Viallet, G. Viau, L. Ressier, *J. Phys. Chem. C*, 2013, **117**, 1935.
43 N. G. Bastús, J. Comenge, V. Puntes, *Langmuir*, 2011, **27**, 11098.
44 C. Fernández-López, C. Mateo-Mateo, R. A. Álvarez-Puebla, J. Pérez-Juste, I. Pastoriza-Santos, L. M. Liz-Marzán, *Langmuir*, 2009, **25**, 13894.
45 A. Van Blaaderen, A. Vrij, *Langmuir*, 1992, **8**, 2921.
46 M. Ferrié, N. Pinna, S. Ravaine, R. A. L. Vallée, *Opt. Express*, 2011, **19**, 17697.
47 A. Taflove, A. Oskooi, S. G. Johnson, Advances in FDTD Computational Electrodynamics: Photonics and Nanotechnology; Artech House, 2013.
48 A. D. Rakic, A. B. Djurisic, J. M. Elazar, M. L. Majewski, *Appl. Opt.*, 1998, **37**, 5271.
49 S. V. Gaponenko, D. V. Guzatov, *Chem. Phys. Lett.*, 2009, **477**, 411.
50 K. Kneipp, H. Kneipp, *Appl. Spectrosc.*, 2006, **60**, 322A.
51 E. Vogel, A. Gbureck, W. Kiefer, *J. Mol. Struct.*, 2000, **550**/**551**, 177.
52 W. Li, P. H. C. Camargo, X. Lu, Y. Xia, *Nano Lett.*, 2009, **9**, 485.
53 K. Li, M. I. Stockman, D. J. Bergman, *Phys. Rev. Lett.*, 2003, **91**, 227402.
54 M. Ringler, A. Schwemer, M. Wunderlich, A. Nichtl, K. Kürzinger, T. A. Klar, J. Feldmann, *Phys. Rev. Lett.* 2008, **100**, 203002.
55 A. M. Gabudean, M. Focsan, S. Astilean, *J. Phys. Chem. C*, 2012, **116**, 12240.